A RELATIVISTICALLY CORRECTED THREE DIMENSIONAL SPACE CHARGE ANALYSIS OF ELECTRON BUNCHING

J. Haimson and B. Mecklenburg
Massachusetts Institute of Technology
Cambridge, Massachusetts

Summary

A technique for evaluating the radial and longitudinal forces present within a moving volume of charge is presented. For an assigned array, based on a given set of initial conditions, the bunch is replaced by a volume mesh comprising a series of cylinders and surrounding annulii. The coordinates of these elements are monitored to provide changing charge distribution and bunch shape information during the trajectory. Owing to the rigorous design requirements of the MIT high duty factor linear accelerator, studies have concentrated on the problems of attaining monochromatic bunches of small dimensions suitable for injection into the accelerator waveguide system.[1] Concomitantly, voltage depression effects and reduction of space charge fields due to the presence of conducting walls are included in this presentation.

Introduction

In general, the limitations imposed by the use of multi-disc cylindrical models for electron bunch analyses[2] are too restrictive for the detailed study of critical regions such as the bunch processing and drifting zones immediately prior to acceleration. A more realistic analysis requires the evaluation of such effects as:

(a) "oil-canning" of the discs due to radial variation of the longitudinal momentum. (While application of the axial longitudinal space charge fields to the peripheral particles introduces little error in the central region of a bunch, it becomes less valid as the terminal regions are approached.)

(b) changing radial charge density within the bunch.

(c) distortion of initially assumed geometries into irregular patterns.

(d) radial dependency of external stimuli, e.g., the radial variation of longitudinal electric field strength over the aperture of prebunching cavities.

(e) the presence of surrounding conducting media from the point of view of longitudinal space charge field reduction as well as potential depression within the bunch.

In principle, by assuming symmetry of rotation, many of these features can be evaluated by adopting a multi-annular model, the expanding and contracting elements of which have independent longitudinal and radial migratory freedom.

Description of Technique

Assumptions and Assignment of Charge Locations

The electron bunch is divided into a multiplicity of cylindrical (representing the central core) and annular volumes, the radial and longitudinal dimensions of which are determined from the initially assigned bunch shape and volume charge density distribution and from the gauge of the mesh. Although a regular bunch geometry is not necessary, it affords a convenient means of (a) prescribing the starting conditions for the mesh spatial coordinates, velocity components, and charge containment, and (b) testing the accuracy of the program by comparing the first set of field computations against known radial and longitudinal distributions. (This is discussed further in a later section.)

The analysis assumes that rotational symmetry is conserved about the beam centerline and that the charge density distribution in the azimuthal direction remains constant. Although not essential, for a prescribed charge distribution and bunch geometry, it was found convenient (especially for energy spectra evaluation) to choose the mesh initial coordinates so that volume elements contained equal charge. For example, in cylindrical or spheroidal bunch models of uniform charge density, when using a mesh of NR radial and NZ equal longitudinal divisions, the radial boundary dimensions (r'_n) are given by

$$r'_n = a\left(\frac{n}{NR}\right)^{1/2}, \qquad n = 0, 1, \ldots NR,$$

where "a" is the maximum radial dimension of either model. The corresponding average radii (r'_{mn}) are given by

$$r'_{mn} = \int \rho'_v r' \, dV' \Big/ \int \rho'_v \, dV'$$

$$= 2a\left[n^{3/2} - (n-1)^{3/2}\right] \Big/ 3(NR)^{1/2}, \qquad n = 1, 2, \ldots NR$$

(The charge per element for the spheroidal model is, of course, 3/2 that of the equivalent circumscribing cylinder of the same total charge.) For spheroidal bunches, volume elements which are not fully contained within the boundary

$$(r'/a)^2 + (z'/c)^2 = 1$$

are treated as follows: When $r'_{mn} \le a\left[1 - (z'_{mn}/c)^2\right]^{1/2}$, the partial mesh charge volume is computed and assigned to this r'_{mn} value. When $r'_{mn} > a\left[1 - (z'_{mn}/c)^2\right]^{1/2}$, the charge is allocated proportionally to the neighboring elements. For the work reported in this paper, the charge distribution within individual elements was assumed to be uniform.

Dependency of Field Evaluation on Mesh Dimensions

When computing the radial and longitudinal field components (E'_r and E'_z) in the rest frame at a location (r'_{mn}, z'_{mn}) representing a given annular element, the radial self field and the components of the fields extending from all other charge volumes are appropriately summated. A rigorous solution of the field distribution for an annular volume of charge involves lengthy evaluation of expressions containing elliptic integrals of the first, second, and third kinds for E'_z and numerical evaluation of double integrals for E'_r. (See Appendix.)

Consequently, since a mesh of N volume elements requires N^2 sets of calculations per step in solving the equations of motion, the replacement of these annular volumes by simpler geometric distributions was investigated so that computation time and complexity could be reduced without introducing significant errors. Typical examples are shown in Figs. 1(a) and (b) where the radial and longitudinal field components due to annular elements of various mesh dimensions are compared against idealized surface and line distributions. These diagrams pertain to a radial mesh location of n = 3 in a model having NR = 5; and the $\Delta r' : \Delta z'$ ratios are based on a constant value of $\Delta r'$.

The radial field comparisons of Fig. 1(a) indicate that the use of a ring or washer as a replacement source for the annular volume is satisfactory for field locations remote from the annulus boundaries. As the field coordinates approach a ring source, however, serious errors are introduced, especially for mesh dimensions of $\Delta r' < \Delta z'$. On the other hand, thin cylindrical shells (not shown on this figure) of radius r'_{mn}, having the same ($\Delta z'$) dimensions as the mesh, provide E'_r fields which are in excellent agreement with all annular element field distributions external and up to the radial boundaries r'_n and r'_{n-1}. For field coordinates within the annular volume, a thin washer of annular breadth $(r'_n - r'_{n-1})$ located in the plane of r'_{mn}, provides an acceptable replacement charge distribution for E'_r calculations. Apart from markedly reducing the computation time, these techniques avoid singularities and enable cross-over (or mesh overlap) occurrences to be evaluated.

The annular volume off-axis E'_z field comparisons of Fig. 1(b) indicate that replacement ring geometry is satisfactory for the indicated range of mesh dimensions, for field locations greater than $3\Delta z'$ from the source. (For mesh ratios of $\Delta r' > \Delta z'$ even shorter distances are acceptable.) For closer field locations, greater accuracy is provided by a washer geometry. Equations pertaining to the Fig. 1 distributions have been included in the Appendix.

In evaluating the on-axis fields, it was unnecessary to idealize the axial cylindrical charge volumes since the exact solution, applicable to any mesh dimension, can be readily obtained from the expression,

$$\Delta E'_z = \frac{q}{2\pi\epsilon_0 \lambda_0^2 \Delta\xi' R_1^2} \times \left[\left[R_1^2 + (\xi' - \xi'_2)^2\right]^{\frac{1}{2}} - \left[R_1^2 + (\xi' - \xi'_1)^2\right]^{\frac{1}{2}} - \left|\xi' - \xi'_2\right| + \left|\xi' - \xi'_1\right|\right] \quad (1)$$

where $\xi' = \gamma\xi$ and ξ is the laboratory frame longitudinal field coordinate normalized to the accelerator RF free space wavelength (λ_0); R_1 and $\Delta\xi' = \xi'_2 - \xi'_1$ define the normalized boundaries of a cylindrical source in the rest frame.

Comparison of Actual and Computed Field Distributions

Several spheroidal models of uniform charge density were used to check the accuracy of the assignment of mesh dimensions (based on equal charge containment) as well as the initial values of radial and longitudinal fields existing within individual elements. The computed E'_r and E'_z components within a 5×10 mesh, representing a 10-mm diameter sphere and a prolate spheroid with a 10-mm minor axis (2a) and a 30-mm major axis (2c) are shown in Figs. 2(a) and (b), respectively. The indicated rest frame values have been extracted directly from the space charge subroutine of the multi-phase orbit program for the linear accelerator. As a result, the units are in E'/Q MV/m/coulomb multiplied by a constant equal to 35×10^{-11}. The actual distribution for these spheroidal bunches, as obtained from the rest frame formulae referenced in the Appendix, are given by:

For the sphere,

$$\frac{E'_z}{Q} = \frac{z'}{4\pi\epsilon_0 a^2} \quad \text{and} \quad \frac{E'_r}{Q} = \frac{r'}{4\pi\epsilon_0 a^2} \quad (2)$$

i.e., linear functions having maxima (for the above example, at a = 0.005 m) of

$$\frac{E'_z}{Q} = \frac{E'_r}{Q} = 3.596 \times 10^8 \text{ MV/m/coulomb} \quad (3)$$

The graphs of Fig. 2(a) compare the space charge program computed values with the corresponding Equation (2) values multiplied by the constant 35×10^{-11}, (e.g., actual maxima $(E'/Q) \times 35 \times 10^{-11} = 0.1259$). For the (a/c = 1/3) prolate spheroid,

$$\frac{E'_z}{Q} = 1.171 \times 10^8 \frac{z'}{c}$$

giving (4)

$$\frac{E'_z}{Q} \times 35 \times 10^{-11} = 0.0410 \frac{z'}{c}$$

and

$$\frac{E'_r}{Q} = 1.602 \times 10^8 \frac{r'}{a}$$

giving (5)

$$\frac{E'_r}{Q} \times 35 \times 10^{-11} = 0.0561 \frac{r'}{a}$$

i.e., these field components are also linear functions having maxima at the terminations of the axes. The Fig. 2(b) graphs compare the field distributions obtained from Equations (4) and (5) with the computed data for the prolate spheroidal bunch. Bearing in mind that the mesh field values refer to the coordinate positions, r'_{mn}, z'_{mn}, it can be seen that with this (5×10) mesh the program provides a satisfactory representation if errors of a few percent are acceptable.

To more accurately reproduce actual beam conditions, several non-uniform charge density models were considered. As an example, Fig. 3(a) illustrates the more practical non-uniform charge distribution given by

$$\rho' = \rho'_0 \left[1 - (r'/a)^2 - (z'/c)^2\right] \quad (6)$$

for a prolate spheroidal bunch of a/c = 1/3. The resulting field distributions along the major and minor axes are compared with the corresponding uniform charge density example of Fig. 2(b) for the same contained total charge.

Space Charge Orbits

The radial and longitudinal space charge forces were transformed from the rest frame to the laboratory frame and applied simultaneously to the equations of motions of all mesh coordinates. The resulting system of differential equations was solved numerically in the time domain[2] using a fourth-order Runge-Kutta routine. A simplified form of these laboratory frame equations, including the effect of a magnetic lens (B_z) can be expressed as follows:

$$\ddot{r} = \left(e E'_r / m_o \gamma^2\right) - r\left(eB_z/2m_o\right)^2/\gamma^2 - \dot{r}\dot{\gamma}/\gamma \qquad (7)$$

Also as

$$\frac{d^2 r}{d\xi^2} = \frac{dr}{d\xi}\frac{\beta}{2\pi}\left(-\frac{2\pi}{\beta^2}\right)\frac{d\beta}{d\xi} + \frac{1}{\omega^2}\ddot{r}\left(\frac{2\pi}{\beta}\right)^2 \qquad (8)$$

Substituting for $\ddot{r}$ and normalizing r ($= R\lambda_o$) we obtain

$$\frac{d^2 R}{d\xi} = \frac{1}{\gamma^2\beta^2}\left[\frac{E'_r}{0.511} - R\lambda_o\left(\frac{eB_z}{2m_o c}\right)^2 - \frac{\gamma}{\lambda_o}\frac{d\gamma}{d\xi}\frac{dR}{d\xi}\right] \qquad (9)$$

Assuming β and γ dependent on the initial electrostatic potentials, and for $\dot{r} \ll \dot{z}$,

$$\frac{d\gamma}{d\xi} = \frac{\lambda_o E_z}{0.511}, \quad \frac{d\omega t}{d\xi} = \frac{2\pi}{\beta} \qquad (10)$$

For more accurate analysis,

$$\frac{d\gamma}{d\xi} = \frac{\lambda o}{0.511}\left[E_z + \gamma E'_r \frac{dR}{d\xi}\right] \text{ for } E_\phi = 0 \qquad (11)$$

and

$$\gamma = \left[1 - \left(\dot{z}^2 + \dot{r}^2 + r^2\dot{\phi}^2\right)/c^2\right]^{-\frac{1}{2}} \qquad (12)$$

Presence of Conducting Walls

The electrostatic potentials and longitudinal space charge fields within the bunch are modified due to the presence of conducting media. These effects were investigated for several bunch geometries, using different diameter injection system drift tubes.

It was assumed that the surrounding concentric walls were of infinite conductivity and that equilibrium conditions had been established between the bunch and the image charges. The rest frame potential distributions and gradients in free space, due to particular bunch geometries, were computed at the location of the wall (r' = b). Table I shows this data for three ratios of drift tube to bunch diameter (2b/2a) and several spheroidal bunch geometries of the same uniform charge density and equal 'a' dimension. The center of the bunch is referenced at z' = 0, r' = 0. Free space potential distributions and gradient curves at r' = b, based on equal bunch charge and the same 'a' dimension, are shown in Figs. 4(a) and (b) for spheroidal bunch dimensions of a/c equal 1/3, 1 and 3.

The free space potentials within the charge volume were depressed to establish a zero potential boundary condition at the wall (all longitudinal field components reduce to zero at the wall). These results, as well as the free space and wall modified longitudinal space charge fields, are compared in Table II for equal uniform charge density (ρ'_v) and the same 'a' dimension. Table II also records the longitudinal and radial variation of the wall modified E'_z field and the electrostatic potential within electron bunches of differing shape, for drift tube to beam diameter ratios of 1.2, 2 and 10.

It can be noted that the potential depression effect results in an initial spread of particle velocities throughout the bunch such that the highest γ_o occurs at the bunch periphery (r' = a, z' = 0), intermediate values are present at the axial terminations (r' = 0, z' = ± c), and the lowest γ_o occurs at the center of the charge volume (r' = 0, z' = 0). As the tube to bunch diameter ratio increases, the potential depression also increases, but the radial variation of particle velocity is reduced. The b/a = 1.2, a/c = 1/3 example has been used in Fig. 4(c) to illustrate the radial dependency of the voltage depression and the energy conversion relationship. As a quantitative example, we can compare an oblate (a/c = 3) and a prolate (a/c = 1/3) spheroidal bunch, each having an 'a' dimension of 5 mm and a surrounding drift tube of 12 mm diameter. The Table II data indicates that at z' = 0, the oblate bunch will be depressed 1890 volts/nanocoulomb on axis and 426 volts/nc at r' = a. The corresponding values for the prolate bunch are 543 and 143 volts/nc.

An example of the marked reduction in the E'_z space charge fields along the length of the bunch, due to the presence of conducting walls, is shown in the comparison of Fig. 4(d). In the above analysis, when evaluating the wall modified E'_z distributions, small first order perturbation was assumed (negligible charge migration within the bunch), and the vector potential contribution was disregarded.

Allowing for the above effects, preliminary results from the space charge program indicate that the achievement of low velocity spread bunches of small dimension is strongly dependent upon suitable choice of b/a.

Acknowledgements

The authors wish to thank Dr. W. Bertozzi and A. C. Hindmarsh for stimulating discussions.

References

1. W. Bertozzi et al., Particle Accelerator Conference, Washington, March 1967.
2. J. Haimson, Nucl. Inst. Meth. 39, 13, January 1966.
3. A. S. Ramsey, An Introduction to the Theory of Newtonian Attraction, Cambridge University Press, 1964.

Appendix

Notation: For convenience in expressing the field components, E_z, and E_r, due to an annular, uniformly distributed charge volume (and its various idealized approximations) with inside radius r_1, outside radius r_2, end planes $z=z_1$ and $z=z_2$, midplane $z=z_m$, and mean radius r_m, the following notation has been adopted:

i	1	2	3	4	5	6	7	8	9	10	11
r_i	r_2	r_1	r_1	r_2	r_m	r_m	r_m	r_m	r_2	r_1	r
z_i	z_2	z_2	z_1	z_1	z_m	z_2	z_1	z	z_m	z_m	z_m

$$k_i^2 = \frac{4r_i r}{A_i}, \quad p_i = \left[r^2+(z_i-z)^2\right]^{1/2}, \quad m_i = \frac{-2r}{p_i+r},$$

$$n_i = \frac{2r}{p_i-r}, \quad A_i = (r_i+r)^2+(z_i-z)^2, \quad B_i = \frac{r_i^2-p_i^2}{A_i^{1/2}},$$

$$C_i = \frac{(z_i-z)^2}{A_i^{1/2}}\left(\frac{p_i+r_i}{p_i-r}\right), \quad D_i = \frac{(z_i-z)^2}{A_i^{1/2}}\left(\frac{p_i-r_i}{p_i+r}\right).$$

$$F(k) = \int_0^{\pi/2} \frac{d\phi}{\left[1-k^2\sin^2\phi\right]^{1/2}}, \text{ elliptic integral of the first kind}$$

$$E(k) = \int_0^{\pi/2} \left[1-k^2\sin^2\phi\right]^{1/2} d\phi, \text{ elliptic integral of the second kind}$$

$$\Pi(n,k) = \int_0^{\pi/2} \frac{d\phi}{\left[1+n\sin^2\phi\right]\left[1-k^2\sin^2\phi\right]^{1/2}}, \text{ elliptic integral of the third kind}$$

Annulus: (total contained charge = q)

$$E_z = \frac{q}{2\pi^2\epsilon_o(r_2^2-r_1^2)(z_2-z_1)} \sum_{i=1}^{4} (-1)^{i+1}\left[A_i^{1/2}E(k_i)+B_iF(k_i) + C_i\Pi(n_i,k_i)+D_i\Pi(m_i,k_i)\right]$$

Ring:

$$E_z = \frac{q}{2\pi^2\epsilon_o}\,\frac{(z-z_m)}{A_5^{3/2}}\,\frac{E(k_5)}{(1-k_5^2)}$$

$$E_r = \frac{q}{4\pi^2\epsilon_o r A_5^{1/2}}\left[F(k_5)+\left(-1+\frac{k_5^2(r+r_m)}{2r_m}\right)\frac{E(k_5)}{(1-k_5^2)}\right]$$

Shell:

$$E_z = \frac{q}{2\pi^2\epsilon_o(z_2-z_1)}\left[\frac{F(k_6)}{A_6^{1/2}} - \frac{F(k_7)}{A_7^{1/2}}\right]$$

$$E_r = \frac{q}{4\pi^2\epsilon_o(z_2-z_1)}\left[\frac{z_2-z_1}{A_6^{1/2}}\left[F(k_6)+\frac{r-r_m}{r+r_m}\Pi(-k_8^2,k_6)\right] - \frac{z_1-z}{A_7^{1/2}}\left[F(k_7)+\frac{r-r_m}{r+r_m}\Pi(-k_8^2,k_7)\right]\right]$$

Washer:

$$E_z = \frac{q(z-z_m)}{2\pi^2\epsilon_o(r_2^2-r_1^2)} \times \left[-\frac{1}{A_9^{1/2}}\left[\frac{p_{11}+r_2}{p_{11}-r}\Pi(n_{11},k_9)+\frac{p_{11}-r_2}{p_{11}+r}\Pi(m_{11},k_9)\right] + \frac{1}{A_{10}^{1/2}}\left[\frac{p_{11}+r_1}{p_{11}-r}\Pi(n_{11},k_{10})+\frac{p_{11}-r_1}{p_{11}+r}\Pi(m_{11},k_{10})\right]\right]$$

$$E_r = \frac{q}{2\pi^2\epsilon_o(r_2^2-r_1^2)r} \times \left[\frac{1}{A_9^{1/2}}\left[-A_9E(k_9)+\left[r_2^2+r^2+(z_m-z)^2\right]F(k_9)\right] - \frac{1}{A_{10}^{1/2}}\left[-A_{10}E(k_{10})+\left[r_1^2+r^2+(z_m-z)^2\right]F(k_{10})\right]\right]$$

Prolate Spheroid: For a prolate spheroid[3] with semiminor axis, a, and semimajor axis, c,

$$\frac{E_z}{Q} = \frac{3z}{4\pi\epsilon_o a^2 c}\,\frac{(1-A^2)}{A^2}\left[-1+\frac{1}{2A}\log_e\left(\frac{1+A}{1-A}\right)\right]$$

$$\frac{E_r}{Q} = \frac{3r}{8\pi\epsilon_o a^2 c}\left[\frac{1}{A^2}-\frac{(1-A^2)}{2A^3}\log_e\left(\frac{1+A}{1-A}\right)\right]$$

where $A^2 = 1-(a/c)^2$.

TABLE I

Ratio of Tube To Bunch Diameter (2b/2a)	Spheroidal Bunch Geometry (a/c)	$(\epsilon_0/a^2\rho'_v)\phi_b$ in Free Space at r' = b			$(\epsilon_0/a\rho'_v)\Delta\phi_b$		
		(z' = 0)	(z' = c/2)	(z' = c)	(z' = c/2)	(z' = 3c/4)	(z' = c)
1.2	1/10 (prolate)	1.1703	.9478	.4452	.0721	.0930	.0723
	1/3	.6326	.5396	.3511	.0878	.1033	.0905
	1 (sphere)	.2778	.2564	.2134	.0546	.0640	.0642
	3 (oblate)	.0990	.0971	.0926	.0149	.0199	.0229
2.0	1/10	.9267	.7661	.4163	.0519	.0643	.0533
	1/3	.4351	.3897	.2933	.0434	.0527	.0518
	1	.1667	.1617	.1491	.0141	.0191	.0223
	3	.0563	.0561	.0554	.0020	.0030	.0039
10.0	1/10	.3074	.2871	.2395	.0069	.0089	.0096
	1/3	.0990	.0980	.0953	.0012		.0022

TABLE II

Ratio of Tube to Bunch Diameter	Spheroidal Bunch Geometry	Potential at r'=0 $(\epsilon_0/a^2\rho'_v)\phi_0$		Potential at r'=a $(\epsilon_0/a^2\rho'_v)\phi_a$	Potential Depression $(\epsilon_0/a^2\rho'_v)\Delta\phi$			Longitudinal Field in Rest Frame $(\epsilon_0/a\rho'_v)E'_z$					
					At Beam Centerline (r'=0)		At Beam Edge (r'=a)	In Free Space			With Wall Present		
(2b/2a)	(a/c)	(z'=0)	(z'=c)	(z'=0)	(z'=0)	(z'=c)	(z'=0)	(z'=c/2)	(z'=3c/4)	(z'=c)	(z'=c/2)	(z'=3c/4)	(z'=c)
1.2	1/10(prolate)	1.5040	.4899	1.2591	.3337	.0447	.0888	.1014	.1521	.2028	.0293	.0591	.1306
	1/3	.9348	.4556	.7120	.3022	.1045	.0794	.1631	.2446	.3262	.0753	.1413	.2356
	1 (sphere)	.5000	.3333	.3333	.2222	.1199	.0555	.1667	.2500	.3333	.1121	.1860	.2691
	3 (oblate)	.2158	.1811	.1253	.1168	.0885	.0263	.1063	.1594	.2126	.0914	.1395	.1897
2.0	1/10	1.5040	.4899	1.2591	.5773	.0736	.3324	.1014	.1521	.2028	.0495	.0878	.1496
	1/3	.9348	.4556	.7120	.4997	.1623	.2769	.1631	.2446	.3262	.1197	.1919	.2743
	1	.5000	.3333	.3333	.3333	.1842	.1667	.1667	.2500	.3333	.1526	.2309	.3110
	3	.2158	.1811	.1253	.1595	.1257	.0690	.1063	.1594	.2126	.1043	.1564	.2086
10.0	1/10	1.5040	.4899	1.2591	1.1966	.2504	.9517	.1014	.1521	.2028	.0945	.1432	.1933
	1/3	.9348	.4556	.7120	.8358	.3603	.6130	.1631	.2446	.3261	.1619		.3239

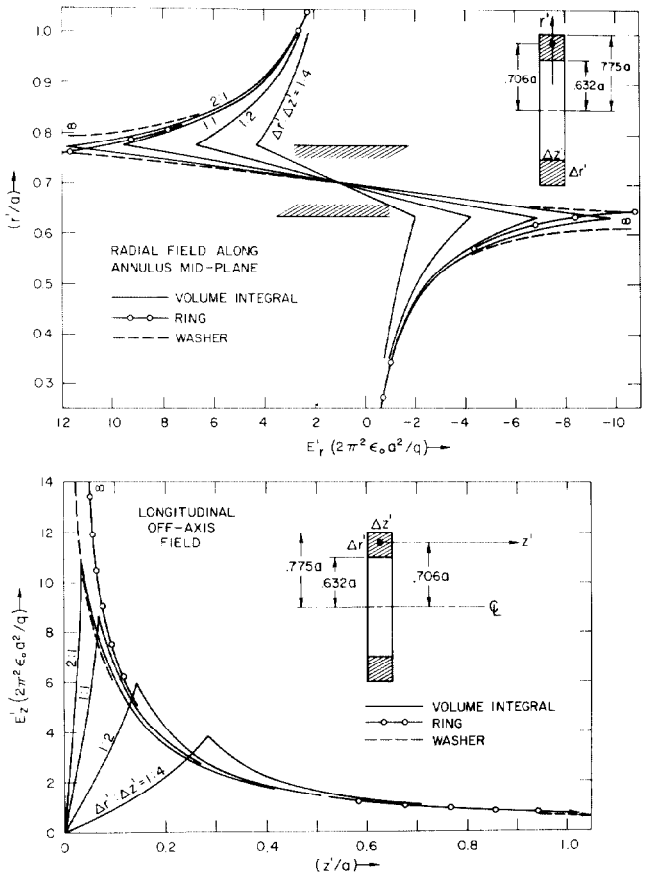

Fig. 1. Comparision of field components of annular and idealized geometries.

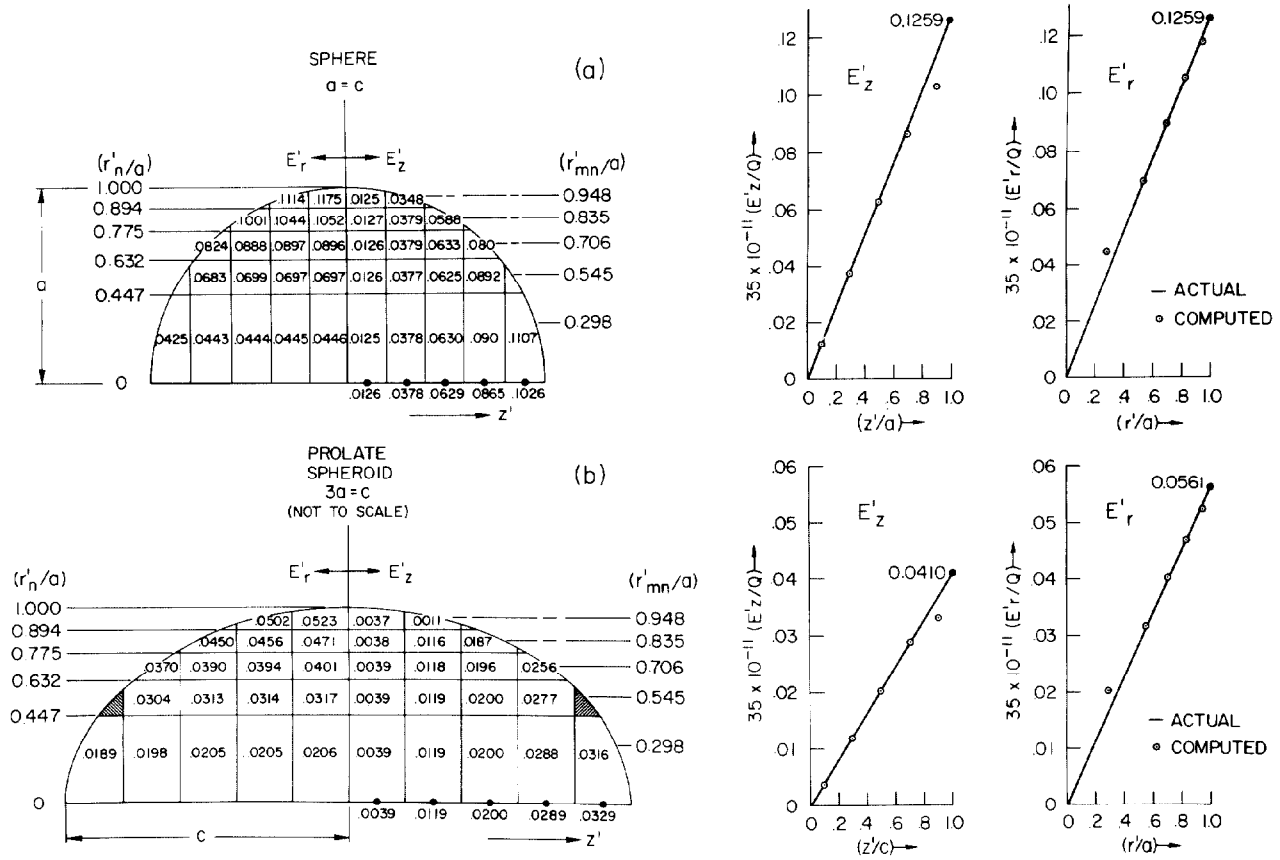

Fig. 2. Comparison of actual and computed field values for spheroidal geometries.

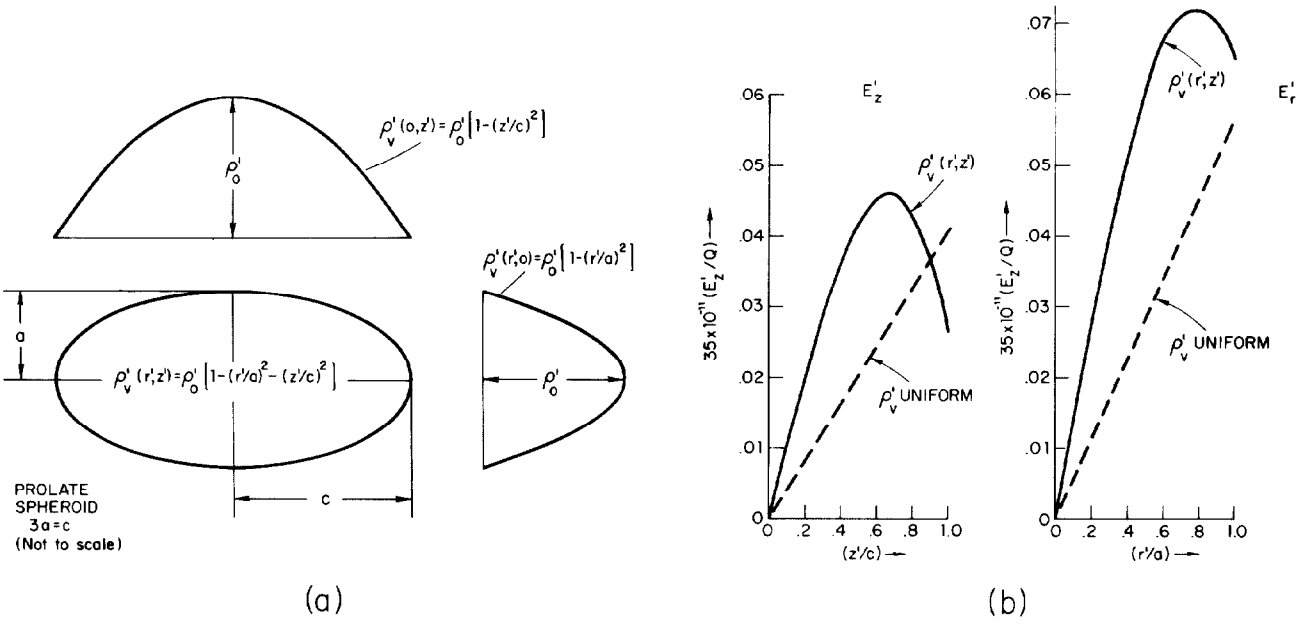

Fig. 3. Field distribution for a non-uniform charge density prolate spheroidal model.

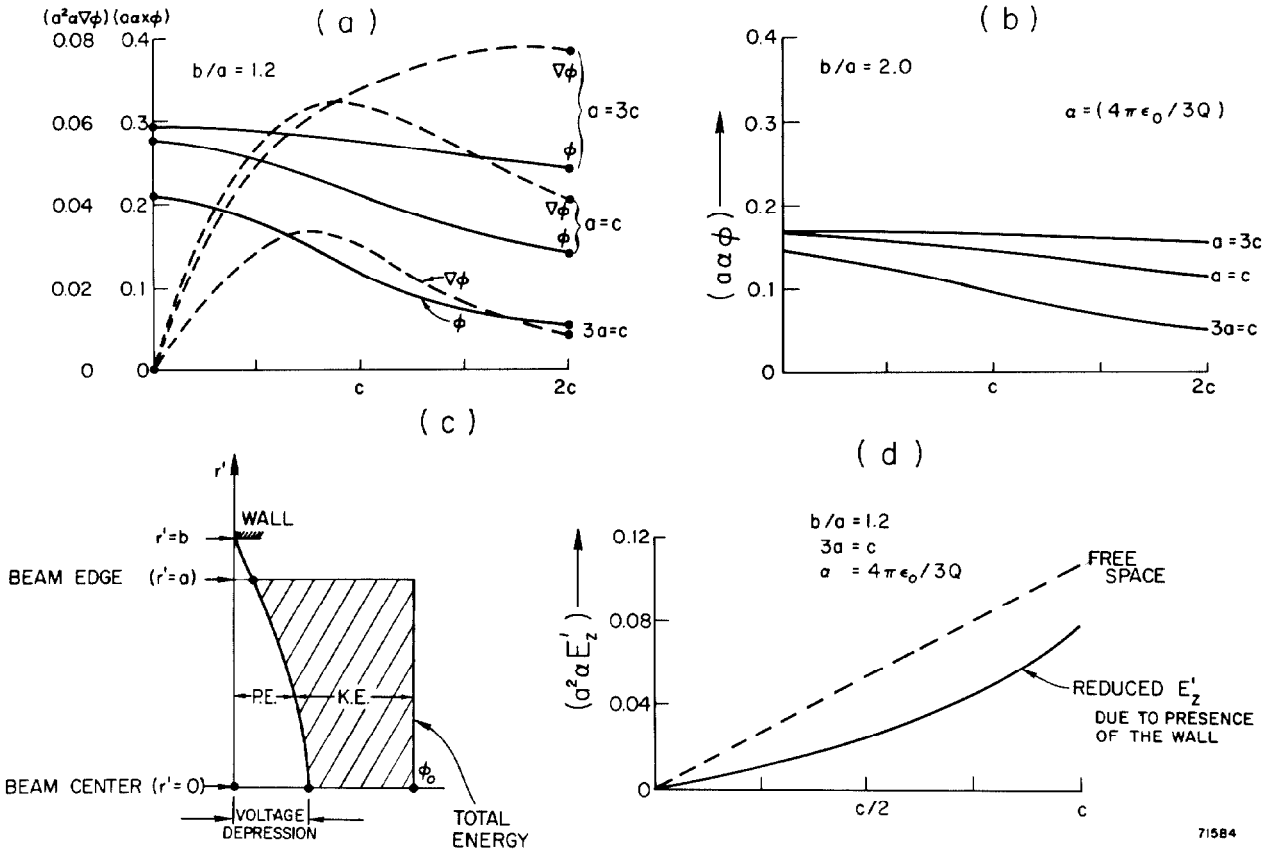

Fig. 4. Potential depression and longitudinal space charge reduction effects due to presence of a conducting wall.